Monthly Notices
of the
ROYAL ASTRONOMICAL SOCIETY

MNRAS **460,** 3563–3569 (2016)
Advance Access publication 2016 May 25

doi:10.1093/mnras/stw1255

Implications of the pulsar wind nebula scenario for a TeV gamma-ray source VER J2016+371

Lab Saha★

Nicoulas Copernicus Astronomical Center, Rabiańska 8, PL-87-100, Toruń, Poland

Accepted 2016 May 23. Received 2016 May 23; in original form 2016 March 22

ABSTRACT

We present multiwavelength studies of a TeV gamma-ray source VER J2016+371 suggested to be associated with a supernova remnant CTB 87 (G74.9+1.2) and based on X-ray and radio morphologies, CTB 87 is identified as an evolved pulsar wind nebula. A source in the vicinity of VER J2016+371 is also detected at GeV energies by *Fermi Gamma Ray Space Telescope* suggesting a likely counterpart at GeV energies. We find that a broken power-law (BPL) distribution of electrons can explain the observed data at radio, X-ray and TeV energies, however, is not sufficient to explain the data at MeV–GeV energies. A Maxwellian distribution of electrons along with the BPL distribution of electrons in low magnetic fields can explain the observed multiwavelength data spanned from radio to TeV energies suggesting this as the most likely scenario for this source. We also find that although the hadronic model can explain the observed GeV–TeV data for the ambient matter density of $\sim$20 cm^{-3}, no observational support for such high ambient density makes this hadronic scenario unlikely for this source.

Key words: pulsars: general – ISM: individual objects (VER J2016+371 CTB 87, FGL J2015.6+3709) – ISM: supernova remnants – gamma-rays: stars.

1 INTRODUCTION

Pulsar wind nebulae (PWNe) are considered to be potential Galactic sources of radiation from radio to very high energy gamma-rays. The non-thermal emission from a pulsar wind nebula (PWN) is believed to result from synchrotron and inverse Compton (IC) radiation of the high-energy particles (leptons) injected from a rotation-powered neutron star in the presence of magnetic field. Detection of such PWNe by the present generation of high-energy gamma-ray telescopes (e.g. *MAGIC*, *HESS*, *VERITAS*) at GeV–TeV energies have revealed them as likely candidates for very high energy gamma-rays (see, e.g. Gaensler & Slane 2006 for a review). Moreover, observed characteristics of many of the unidentified GeV sources by *Fermi Gamma Ray Space Telescope* (*Fermi-LAT*), also detected at TeV energies, are similar to those of well-known PWNe (see, e.g., Kargaltsev, Rangelov & Pavlov 2013 for a review).

A TeV source VER J2016+371 has been recently resolved at TeV energies by *VERITAS* telescope system (Aliu et al. 2014) as a point source. This source has been detected with a statistical significance of $\sim$5.8σ with measured integral energy flux of $(8.2 \pm 3.4_{\rm stat} \pm 2.9_{\rm sys}) \times 10^{-13}$ erg cm^{-2} s^{-1} between 1 and 10 TeV (Aliu et al. 2014). This is positionally coincident with a supernova remnant (SNR) CTB 87 (G74.9+1.2) which is a centrally brighten SNR with no evidence of an SNR shell (Dickel & Denoyer 1975; Duin et al. 1975; Wallace et al. 1997). Detailed analysis of the X-ray data of CTB 87 from *Chandra* has discerned its morphology as an evolved PWN with a putative pulsar residing at southeast to the remnant centre (Matheson, Safi-Harb & Kothes 2013). A *Fermi-LAT* GeV source 3FGL J2015.6+3709 is positionally close to VER J2016+371. Although it has been associated with a blazar B2013+370 behind the Galactic plane (Kara et al. 2012; Acero et al. 2015), GeV association with VER J2016+371 cannot be suppressed due to low angular resolution at GeV and TeV energies compared to radio and X-ray energies.

In a PWN scenario, observed emissions from radio to X-rays are normally explained by the synchrotron radiation process, whereas the observed fluxes at GeV–TeV energies are explained by IC emission mechanism with synchrotron photons, dust photons, and cosmic microwave background (CMB) photons. A well-known example of such systems is the Crab Nebula whose emission extends from radio to very high energy gamma-rays (see Hester 2008 for a review). The observed emission spectrum from the Crab Nebula is well explained by the synchrotron radiation and IC processes (de Jager & Harding 1992; Atoyan & Aharonian 1996; Hillas et al. 1998; Bednarek & Bartosik 2003). In general, it is believed that for the old PWNe the IC scattering with dust photons and CMB (hereafter IC-CMB) photons are dominant process at high energies, however IC with synchrotron photons (hereafter SSC) arising from the same population of electrons becomes dominant for young PWNe like the Crab Nebula. In an alternative scenario for electrons, bremsstrahlung process can significantly contribute to photons at

★ E-mail: labsaha@ncac.torun.pl

high energies depending upon the density of the ambient medium. In addition to electrons, high-energy protons (primarily heavy nuclei) may be accelerated (Atoyan & Aharonian 1996; Bednarek & Protheroe 1997; Bednarek & Bartosik 2003; Amato, Guetta & Blasi 2003), which can produce GeV–TeV photons through decay of neutral pions (π^0s) produced in inelastic p–p collisions. Although the Crab Nebula is considered as a prototype PWN, the number of PWNe whose morphologies, energetics, spectral indices are quite different from that of the Crab Nebula, is continuously increasing, thus forming a different class of PWNe. Multiwavelength studies of these sources can provide significant information about the injected particle spectrum, dominant emission processes and magnetic fields in the emission volume.

In this paper, we study VER J2016+371 at MeV–GeV energies considering data from *Fermi-LAT* in the region around this. In addition, we study the implications of a scenario in which observed radio, X-ray, and GeV emission are considered to be associated with the TeV emission from VER J2016+371, and they arise from a PWN type source. We find that a simple power-law (PL) distribution of electrons is not sufficient to explain the observed spectrum at GeV–TeV energies. The observed gamma-rays at TeV energies can be partially explained by IC-CMB[1] process. However, the observed fluxes at MeV–GeV energies cannot be fitted well with either by SCC or by IC-CMB processes indicating requirements for a different type of electron spectrum in the emission volume. We find that a broken power-law (BPL) electron distribution can explain the observed data at TeV energies well. However, MeV–GeV data remains unexplained with this BPL electron distribution. A Maxwellian population of electrons together with the BPL distribution of electrons can explain the observed multiwavelength data well suggesting this as the most likely scenario for VER J2016+371. In addition to synchrotron and IC spectra, we also consider both bremsstrahlung and π^0-decay processes to account for the observed data at GeV–TeV energies. Although bremsstrahlung process cannot explain the observed data at high energies, π^0-decay process can explain the GeV–TeV data well for an assumed ambient density of $\sim$20 cm^{-3} which is, however, unlikely for this PWN. These scenarios and their implications are discussed more quantitatively in the following sections within the framework of a PWN scenario.

The rest of the paper is organized as follows; First, in Section 2 we discuss details of data analysis of *Fermi-LAT*. In Section 3 we calculate the multiwavelength photon spectra to explain the observed multiwavelength data. We discuss the results and the implications resulting from the multiwavelength studies in Section 4. Finally, we summarize our results and conclude in Section 5.

2 DATA ANALYSIS AND RESULTS

Fermi-LAT data for VER J2016+371 taken in the period between 2011-01-01 (MJD 55562) and 2015-08-01 (MJD 57030) are analysed in this study. All gamma-ray events taken from a circular region of interest (ROI) with radius 15° centred at the position of RA(J2000) = $20^h16^m02^s$ and Dec(J2000) = $37°11'52''$ are extracted. We select the events suggested for *Fermi-LAT* Pass 8 analysis for Galactic point sources using *gtselect* of Fermi Science Tools (FST; v10r0p5). In order to prevent event contamination at the edge of the field of view due to the bright gamma-rays from the Earth's limb, gamma-ray events with reconstructed zenith angles greater than 105° are rejected. We use standard binned likelihood analysis. For spectral analysis of the data, the gamma-ray events are binned in energy at eight logarithmic steps between 100 MeV and 300 GeV. To correctly model the background we consider all the sources within our ROI from the 3rd *Fermi-LAT* (3FGL) catalogue. Since the point-spread function of LAT is large, we also consider sources from the region 10° away from the ROI to account for emission at low energies (Abdo et al. 2009). Considering this extended region of the sources, exposure map, which depends on orientation, orbit location, pointing direction and live time of the data accumulation, are produced. For spectral modelling, we use the newly introduced instrument response function *P8R2_SOURCE_V6*. The diffuse Galactic emission (gll_iem_v06.fits) and isotropic emission models (iso_P8R2_SOURCE_V6_v06.txt) are used for the binned likelihood analysis using the *gtlike* tool of FST. To determine the best set of spectral parameters of the fit, the parameters of the 3FGL sources within 3° around VER J2016+371 are varied. We keep all the parameters of *Fermi-LAT* 3FGL sources fixed, which are more than 3° away from the centre of the ROI. In this work, we use PYTHON based software ENRICO (Sanchez & Deil 2013) for *Fermi-LAT* analysis.

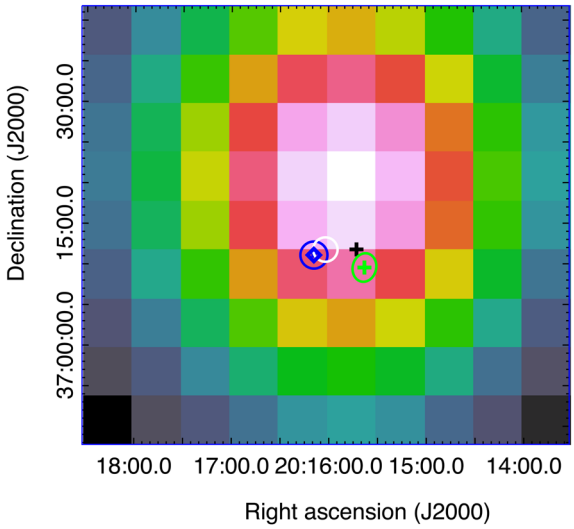

Figure 1. Gamma-ray TS map of the source considered to be associated with VER J2016+371. The best-fitting position of the source obtained with *gtfindsrc* of Fermi tools is shown with a black cross. The green cross represents the 2nd Fermi- LAT catalogue source with an error ellipse (green) with 95 per cent confidence. The blue diamond represents the best-fitting position of the putative pulsar with a blue circle for the diffuse nebula. The dashed white circle indicates the systematic uncertainty of $\sim$ 1.5 arcmin (Aliu et al. 2014) in the best-fitting position of VER J2016+371. (A color version of this figure is available in the online journal.)

We have detected a source (positionally coincident with VER J2016+371) with a statistical significance of $\sim 36\sigma$ using binned likelihood analysis. The best-fitting position within the ROI of VER J2016+371 obtained using *gtfindsrc* tool of FST is found to be longitude, $l = 303.928 \pm 0.01$ and latitude, $b = 37.1969 \pm 0.01$. The model is then refitted using the best-fitting position to compute the TS map and differential energy spectrum. The TS map is shown in Fig. 1 with a cross (black) which indicates the best-fitting position. The statistical positional uncertainty of VER J2016+371 estimated by *VERITAS* is shown with a dashed white circle. The X-ray peak position is shown with a diamond (blue). The position of the source 3FGL J2015.6+3709 from 3FGL catalogue is shown with a cross

[1] In the IC-CMB contribution we have included both CMB photons and photons from interstellar radiation field (taken from Mathis, Mezger & Panagia 1983).

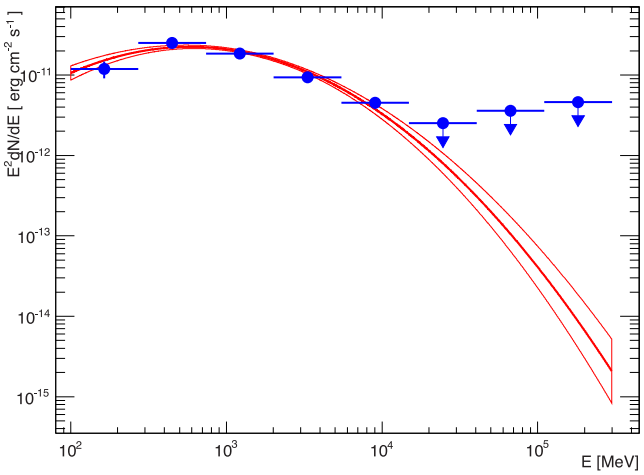

Figure 2. *Fermi-LAT* spectrum of the source considered to be associated with VER J2016+371. The best-fitting curve along with 1σ error bars are shown with solid lines. The parameters of the fit for LP model is given in the text. (A color version of this figure is available in the online journal.)

(green) with an error ellipse (green) of 95 per cent confidence. The best-fitting position of the source obtained in this analysis is separated by 0.°04 from the *Fermi-LAT* source 3FGL J2015.6+3709 and shifted towards the best-fitting positions at X-rays and TeV gamma-rays as clearly seen from Fig. 1. The source spectral energy distribution (SED) of VER J2016+371 at MeV–GeV energies is shown in Fig. 2 and is best described by a log parabola (LP) function between 100 MeV and 300 GeV. The functional form of the LP is shown in equation (1):

$$\frac{\mathrm{d}F}{\mathrm{d}E} = N_{\mathrm{o}}(E/E_{\mathrm{b}})^{-(\Gamma_1+\Gamma_2\ \ln(E/E_{\mathrm{b}}))}. \quad (1)$$

The best-fitting parameters for the LP model are $N_{\mathrm{o}} = (4.85 \pm 0.22) \times 10^{-12}$ MeV^{-1} cm^{-2} s^{-1}, $\Gamma_1 = 2.45 \pm 0.46$, and $\Gamma_2 = 0.23 \pm 0.03$ and $E_{\mathrm{b}} = 1522$ MeV, where the given uncertainties are statistical. The total flux is found to be, $F(>100\ \mathrm{MeV}) = (1.01 \pm 0.01) \times 10^{-7}$photons cm^{-2} s^{-1}.

3 MULTIWAVELENGTH MODELLING

For multiwavelength modelling of VER J2016+371 we use published radio fluxes at different radio frequencies (Pineault & Chastenay 1990; Wendker, Higgs & Landecker 1991; Kothes et al. 2006; Sun et al. 2011). X-ray data and GeV–TeV data are taken from Matheson et al. (2013) and Aliu et al. (2014), respectively. For X-ray data, we consider the total X-ray flux 1.8×10^{-12} erg cm^{-2} s^{-1} as an upper limit from the extended diffuse nebula of size ∼200 arcsec × 300 arcsec (Matheson et al. 2013). The observed fluxes at MeV – GeV energies are taken from the results as given in Section 2. The distance to the source is considered as 6.1 kpc (Kothes et al. 2003).

We first consider a leptonic scenario to explain the observed data. For simplicity, a single population of electrons is considered. We assume a simple PL form of distribution of electrons ($\sim\gamma^{-\alpha}\exp[-\gamma/\gamma_{\mathrm{max}}]$) with a high-energy cutoff at $E_{\mathrm{max}} = \gamma_{\mathrm{max}} m_{\mathrm{e}} c^2$.

In general, the electron spectrum may be more complicated than the single power-law form. For the Crab Nebula, two different population of electrons are considered, namely, radio electrons and wind electrons. Radio electrons are less energetic electrons which reside in the nebular volume throughout its age, and they are mostly responsible for the observed radio fluxes. On the other hand, wind electrons are freshly accelerated electrons and they account for the observed fluxes at X-ray and GeV–TeV energies. In the case of the Crab Nebula, low-energetic photons from radio synchrotron nebula are upscattered by the wind electrons giving rise to high-energy photons at GeV–TeV energies. Unlike Crab-like young PWNe, for relic PWNe, the high-energy photons are produced by the up-scattering of CMB photons along with photons from stellar dust contribution since the density of radio photons is low in the emission volume.

In order to explain the observed spectrum for VER J2016+371, we first account for the observed radio fluxes for magnetic field (B) ∼ 55 μG as estimated by Matheson et al. (2013). The calculated synchrotron spectrum is shown in Fig. 3 and the parameters of the fit are shown in Table 1. The peak of the synchrotron spectrum depends on the maximum energy of the electrons, and very often it is restricted by the peak of the observed X-ray spectrum. In this case, we use the total X-ray flux as an upper limit in the energy band 0.3–10 keV. Hence, the maximum energy of the electrons cannot be defined well. However, we choose the maximum energy of the electrons in such a way that the calculated fluxes at X-ray energies do not overestimate the observed fluxes. In order to explain the GeV–TeV data, we calculate spectrum resulting from the IC-CMB mechanism, and we see that this electron population is unable to explain the observed GeV–TeV data through IC-CMB spectra as evident from Fig. 3. For the magnetic field of 55 μG, the calculated fluxes are much less than the observed fluxes at GeV–TeV energies. It is also evident from Fig. 3 that the shape of the IC spectrum is quite different from the observed spectrum. Hence, a simple power-law distribution is not sufficient to explain the observed fluxes at GeV–TeV energies.

Since, for evolved PWNe, the magnetic field strength in the nebular volume is normally considered to be much less (∼5–10 μG) than that for young PWNe (> 100 μG), we also calculate synchrotron and IC spectra for the magnetic field of 10 μG. The best-fitting spectrum, for this case, is also shown in Fig. 3 and parameters of this model is shown in Table 1. Although IC contribution is unable to account for the GeV–TeV data (see Fig. 3), it is significantly increased, which suggests that the lower value of the magnetic fields in the emission volume is preferred for this source and consistent with other evolved PWNe (Slane et al. 2010 and references therein).

Normally, in the leptonic scenario, non-thermal bremsstrahlung process is introduced to explain the data at high energies when IC process fails to do so. Since IC spectrum cannot explain the observed data for the PL electron population, as shown above, we invoke bremsstrahlung process. The density of the ambient medium, however, is required to calculate the contribution from bremsstrahlung process. Matheson et al. (2013) estimated the density of the medium to be $<0.2\,\mathrm{cm}^{-3}$ based on the observed absence of an SNR shell. For this estimated density of ambient medium, bremsstrahlung process cannot explain the observed fluxes at high energies for both the scenarios with the magnetic field values 55 and 10 μG as shown in Fig. 3. Since bremsstrahlung spectrum linearly depends on the density of ambient medium, a higher density (20–100 cm^{-3}) can significantly increase the contribution to the level of GeV–TeV fluxes. However, the shape of the spectrum does not match well with the observed one as evident from Fig. 3.

Since a PL electron spectrum cannot explain the observed data at GeV–TeV energies, we consider a BPL type electron distribution as given by

$$\frac{\mathrm{d}n_{\mathrm{e}}}{\mathrm{d}\gamma} \propto \begin{cases} \gamma^{-\beta} & \text{for } \gamma < \gamma_{\mathrm{br}} \\ \gamma^{-\lambda}\exp\left(-\frac{\gamma}{\gamma_{\mathrm{c}}}\right) & \text{for } \gamma_{\mathrm{br}} \le \gamma \le \gamma_{\mathrm{c}}. \end{cases} \quad (2)$$

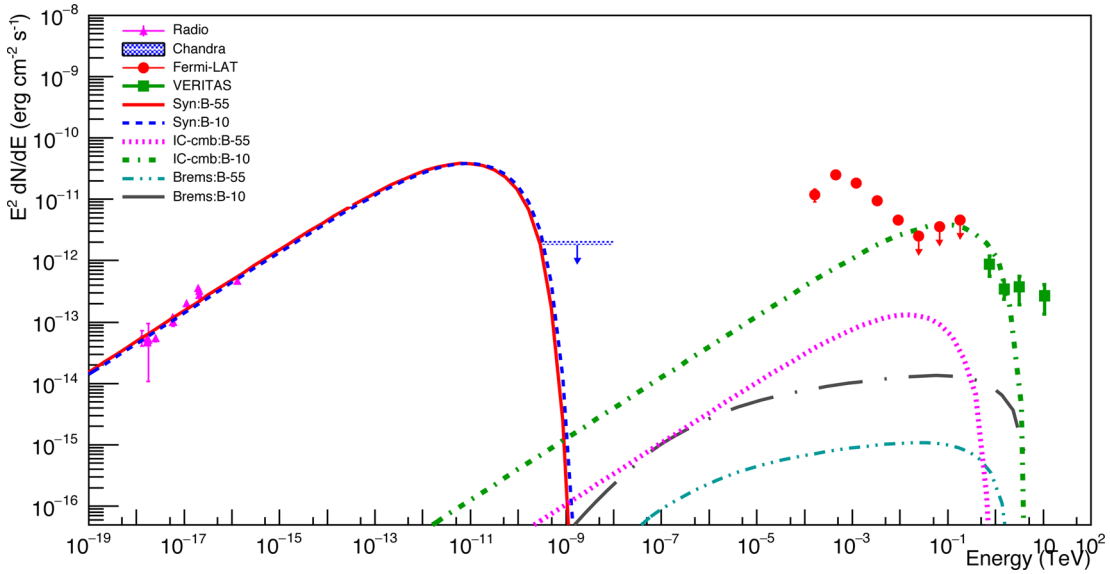

Figure 3. The spectral energy distribution of VER J2016+371 from radio to TeV energies in the PWN scenario for the magnetic fields of 55 and 10 μG. Radio data and X-ray data are explained by synchrotron spectra for both these magnetic field values as shown with solid and dashed lines (marked by the key 'B-55' for $B = 55$ μG and 'B-10' for $B = 10$ μG), respectively. The IC-CMB spectra for both these cases are shown with dotted and dot–dashed lines, respectively. The bremsstrahlung spectra for these magnetic field values are shown with a double-dot–dashed and long-dashed–dot lines, respectively, for the ambient matter density of 0.2 cm^{-3}. (A color version of this figure is available in the online journal.)

Table 1. Fit parameters for a PL model for two different magnetic fields.

Parameters	$B = 55$ μG	$B = 10$ μG
Spectral index (α)	2.0	2.0
Low-energy cutoff ($\gamma_{\rm min}$)	1.0	1.0
High-energy cutoff ($\gamma_{\rm max}$)	3.5×10^6	9.0×10^6
Total energy (10^{48} ergs)	1.13	14.1

Table 2. Fit parameters for a BPL model.

Parameters	Values
Spectral index (β)	2.0
Spectral index (after break) (λ)	3.8
Low-energy cutoff ($\gamma_{\rm min}$)	1.0
High-energy cutoff ($\gamma_{\rm c}$)	3.3×10^8
Break position ($\gamma_{\rm br}$)	2.8×10^6
Magnetic field [B(in μG)]	7
Total energy (10^{49} ergs)	1.9

We calculate the synchrotron and IC-CMB spectra for this type of electron distribution. The model parameters are shown in Table 2 and corresponding SED is shown in Fig. 4. It is clearly illustrated in Fig. 4 that the IC-CMB spectrum can explain the observed gamma-rays at TeV energies (the magnetic field is adjusted to ∼7μG), however, it underpredicts fluxes at MeV–GeV energies. Similar characteristics in the SEDs are observed in two evolved PWNe Vela X (LaMassa, Slane & de Jager 2008; Grondin et al. 2013) and HESS J1640-465 (Slane et al. 2010), where the simple power-law (or BPL) distribution of electrons fails to account for the observed fluxes, specifically, at MeV–GeV energies. To explain the observed *Fermi-LAT* data for HESS J1640 at MeV–GeV energies, a Maxwellian distribution of electron population was chosen (Slane et al. 2010). Such a particle spectrum was obtained in a particle-in-simulations study in the downstream of the wind termination shock (Spitkovsky 2008). Hence, we consider a Maxwellian population of electrons ($\propto \gamma \exp[-\gamma/\delta\gamma]$) as an additional component to the BPL electron distribution. Fig. 4 illustrates that a Maxwellian distribution of electron with $\delta\gamma = 1.5 \times 10^5$ can explain the observed flux well at *Fermi-LAT* energies, where BPL model fails. We also calculate bremsstrahlung spectra for both these electron distributions (BPL and Maxwellian), and we find that none of them can account for the observed fluxes for the ambient density of 0.2 cm^{-3}.

As mentioned in the Introduction, although SSC is the dominant emission process for young PWNe, for evolved PWNe, it can contribute significantly when the emission region is considered very compact (Saha & Bhattacharjee 2015). For this case, even if we consider that the emission is coming from the compact nebula of angular size ∼5 arcsec (≃ 0.15 pc at a distance 6.1 kpc), it is not sufficient for SSC to become a dominant process. In addition to the leptonic scenario, we also introduce hadronic scenario as an addition component which mostly contributes to very high energies (MeV–TeV). We calculate gamma-ray spectrum resulting from the decay of neutral pions following Kelner, Aharonian & Bugayov (2006). The gamma-ray spectrum for the relativistic protons with $dN/dE \propto E^{-2.55}$ with a spectral break at 100 TeV for an ambient gas density of $n_{\rm H} \simeq 20$ cm^{-3} is shown in Fig. 5. The total energy can be calculated as $W_{\rm p} = 3.26 \times 10^{50} \times (20.0/n_{\rm H})$ ergs. It is evident from the figure that the gamma-ray spectrum resulting from the decay of neutral pions can explain the observed GeV–TeV data very well. However, this ambient density is much higher than that the limit on the density of ambient medium of 0.2 cm^{-3} as suggested by (Matheson et al. 2013). In general, such high densities are found in dense molecular clouds. There could be two different scenarios in SNR for the interaction of molecular clouds. In the first one, one can assume that the clumpy molecular cloud could be present inside the SNR volume leading to p–p collisions. In the second scenario, it is considered that the relativistic protons already escaped the

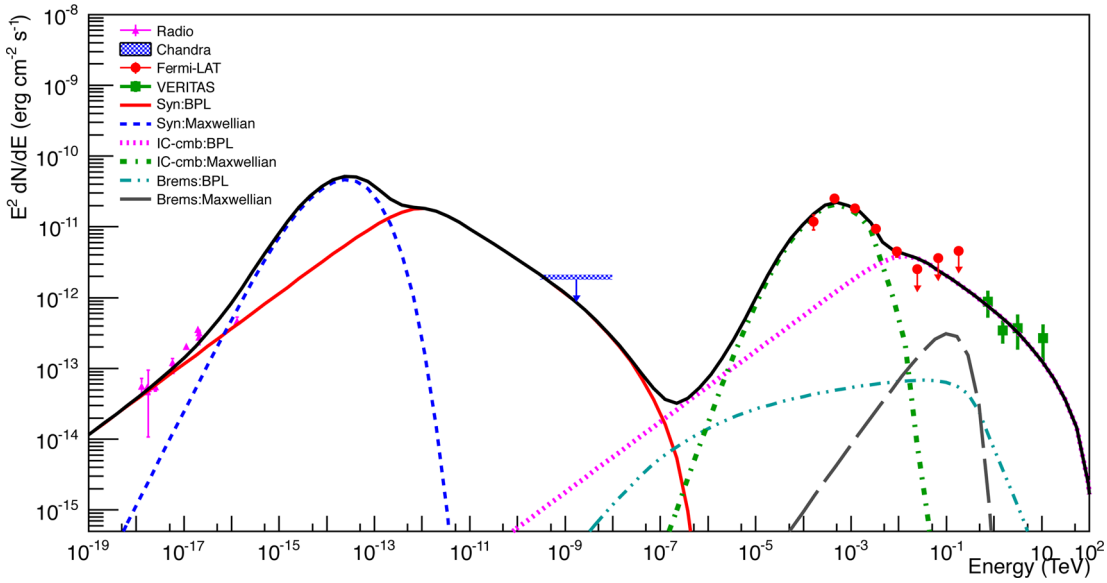

Figure 4. Same as Fig. 3 but only for the different population of electrons. The synchrotron and IC spectra for a BPL distribution of electrons (marked by the key 'BPL') are shown with solid and dotted lines, respectively. The dashed and dot–dashed lines are synchrotron and IC spectra, respectively, for a Maxwellian distribution of electrons (marked by the key 'Maxwellian') with mean $\gamma = 1.5 \times 10^5$. The bremsstrahlung spectra for the BPL and Maxwellian electron distributions are shown with double-dot–dashed and long dashed lines, respectively, for the ambient matter density of 0.2 cm^{-3}. The thick solid line corresponds to combined fit to the data for these distributions of electrons. (A color version of this figure is available in the online journal.)

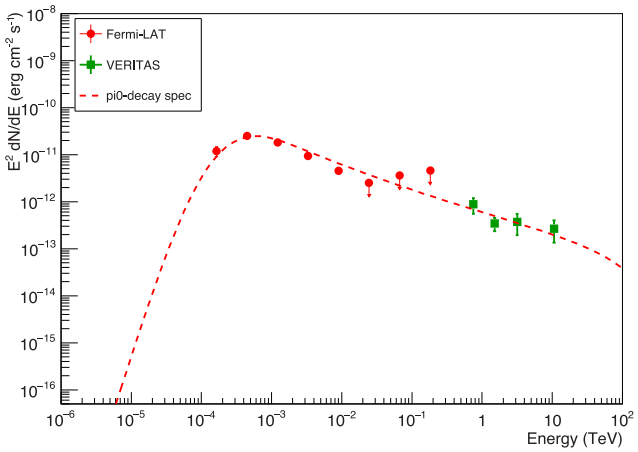

Figure 5. Gamma-ray spectrum resulting from the decay of neutral pions. The best-fitting spectrum is calculated for the ambient proton density of 20 cm^{-3}. (A color version of this figure is available in the online journal.)

acceleration region and interact with molecular cloud outside the SNR volume. In this case, the total energy of protons requires to be unreasonably higher than that mentioned above ($\sim 10^{50}$ ergs) since the accelerated protons will lose a significant amount of energy while escaping from the SNR volume. Although a reasonable value of the total energy can be considered for the protons escaping the SNR volume, the ambient matter density in the molecular cloud has to be much higher than that mentioned above ($\sim$20 cm^{-3}). Moreover, the second scenario needs supports from observation where GeV–TeV emission should come from a region different from the peak of radio and X-ray positions. Such observational supports for none of the cases mentioned above for the second scenario are present. In case of the first scenario, the presence of the dense molecular cloud (with ambient matter density of $\sim$20 cm^{-3}) in the SNR volume can significantly contribute to the fluxes at GeV–TeV energies. However, such a dense medium will be responsible for limb-brightened morphology for this PWN, which is not observed so far. Hence, both the scenarios within the context of hadronic model are unlikely. Nevertheless, for a less dense medium contribution from this scenario to total observed fluxes to some extent cannot be ruled out.

4 DISCUSSION

The observed multiwavelength spectrum of VER J2016+371 is studied considering both leptonic and hadronic scenarios which reveal some interesting characteristics of this source. We have seen that a simple PL distribution of electrons cannot explain the observed data at MeV–TeV energies. We have also found that although a BPL type of electron distribution can explain the data at TeV energies, the observed spectrum at MeV–GeV energies remains unexplained. However, a BPL type electron distribution and a Maxwellian population of electrons together can explain data well at MeV–TeV energies suggesting this as most likely scenario for this source. In the leptonic scenario, the magnetic field of $\sim$10 μG is more preferable than the magnetic field estimated to be 55 μG by Matheson et al. (2013). From the spectral parameters of the fit to the data in the extended nebular region, it can be seen that the magnetic energy density is much lower than the particle energy density, which implies that the equipartition of magnetic energy and particle energy is not obeyed in this PWN. This is consistent with other evolved PWN such as Vela X and HESS J160-465, where equipartition between magnetic energy and particle energy is not valid suggesting that magnetic energy has already converted into particle energy over its long lifetime. Spatial distribution of magnetic field in the nebular volume is considered constant for this study. However, the magnetic field may depend on the distance from the central region of the nebula. A constant magnetic field throughout the nebular volume, however, is a good approximation. Moreover, in the context of a leptonic scenario of an evolved PWN, the shape of the

electron spectrum changes due to adiabatic and IC loss, which in turn changes the photon spectrum at GeV–TeV energies (Zhang et al. 2008; de Jager et al. 2009). We see that the IC processes cannot account for the observed spectrum in the scenarios with a PL electron distribution making the consideration of the losses insignificant. However, for the BPL model, since IC contribution becomes relatively significant, there will be some effects on the spectral shape at TeV energies, which can be adjusted with a different choice of parameters. For an evolved PWN the magnetic field is considered to be much less ($\sim$10 μG) than that considered for young PWN like the Crab Nebula ($\sim$125 μG), which yields higher gamma-ray flux relative to X-ray and radio fluxes. For VER J2016+371 the observed radio and X-ray fluxes are less than the fluxes at very high energies making it a likely PWN with the magnetic field of few microgauss.

In addition to synchrotron and IC contribution to the observed fluxes, we have considered bremsstrahlung process which can contribute to high energies. For the estimated matter density of 0.2 cm^{-3}, the bremsstrahlung contribution to high-energy photons is not significant for any of the leptonic scenarios as mentioned above. Although bremsstrahlung spectrum can reach to the level of GeV–TeV fluxes for relatively higher values of ambient gas density, the shape of the spectrum is quite different from the observed spectrum for all the different electron distributions (PL, BPL, and Maxwellian) making it a insignificant process for very high energy photons for this PWN.

In addition to the leptonic model, we have also considered hadronic model to explain the observed data at GeV–TeV energies. Any compelling evidence for acceleration of protons in SNR can be obtained from the observed features in the spectrum at MeV –GeV energies, particularly when the spectrum falls steeply below $\sim$200 MeV (Ackermann et al. 2013). We have seen that the observed spectrum is very well fitted by the π^0-decay gamma-ray spectrum for an assumed matter density of $\sim$20 cm^{-3}. The presence of molecular cloud in the close proximity of VER J2016+371 can strongly support this scenario. Kothes et al. (2003) found evidence of an association of CTB 87 with a molecular cloud present towards the east of CTB 87. However, the density may not be as high as $\sim$20 cm^{-3} since no limb-brightened morphology or any shell structure was seen for this source which can establish that the system evolves in a dense medium. Hence, hadronic scenario is less likely for this source. It is important to note that for a less dense medium hadronic process can contribute, although less significantly, to the total observed fluxes at MeV–TeV energies.

From the radio and X-ray observations, it is established that there is an offset of about 100 arcsec from radio peak to X-ray peak (Matheson et al. 2013). The electron distribution before the break in the BPL model is responsible for explaining the radio data and this is similar to less energetic radio electrons of the Crab Nebula. On the other hand, the electrons corresponding to the distribution after the break are more energetic and are responsible for explaining data at X-ray energies. This is also similar to the wind electrons as considered for the Crab Nebula. For the Crab Nebula, radio electrons and wind electrons are considered to be two different population from two different regions and they are responsible for observed fluxes from radio to gamma-rays (Aharonian & Atoyan 1995; Meyer, Horns & Zechlin 2010). In this case also, one can consider that two different population of electrons from two different regions together form the BPL type electron distribution and this could be a possible reason for the shift between X-ray and radio peaks.

We have considered the total X-ray flux from the diffuse nebula as an upper limit in the energy band of 0.3–10 keV for multiwavelength modelling of this source. However, the observed total X-ray spectrum from the PWN is fitted well with a power-law spectrum with spectral index <2 as reported by Matheson et al. (2013). Although the absence of any significant emission at low X-ray energies indicates that the observed X-ray flux is of non-thermal origin, contribution from emission of thermal origin cannot be ignored, for the limited sensitivity and field coverage of the X-ray observation (Matheson et al. 2013). The presence of thermal-emission in the total observed fluxes may significantly change the spectral shape of the X-rays. Hence, we consider the observed total flux as an upper limit. The observed X-ray spectrum with spectral index <2 can be explained with the same population of electrons (PL or BPL) which explains radio data, depending on the level of X-ray flux compared to radio flux and on the spectral shape of the radio spectrum. On the other hand, the X-ray spectrum with spectral index >2 can be easily explained with the falling edge of the synchrotron component of a PL or a BPL model. We note that the observed spectral indices of the X-ray spectra of the nebula for both the evolved PWNe Vela X and HESS J1640-465 (>2) are quite harder than that for VER J2016+371 (<2). As a result, a single zone model is sufficient to explain the observed radio and X-ray data for Vela X and HESS J1640−465 (Slane et al. 2010; LaMassa et al. 2008). It should also be noted that maximum or cutoff energy of the electrons can be normally obtained by the spectral steepening at X-ray energies. However, for this source, we do not see such shape in X-ray energies between 0.3 and 10 keV. Moreover, we have used total X-ray flux as an upper limit at these energies. Thus, the maximum energy of electrons is not constrained. Nevertheless, IC mechanism can be used to restrict the maximum energy of electrons if the observed fluxes are explained by this emission process (as in the case of BPL model).

It is important to note that *VERITAS* source VER J2016+371 is positionally associated with 3FGL J2015.6+3709 which is considered to be associated with an FSRQ of unknown redshift (Acero et al. 2015). Based on the variability index of the Fermi-LAT source and its correlation with radio, Kara et al. (2012) associated the high-energy gamma-ray emission with the nearby blazar B2013+370, with unknown redshift. However, very high energy gamma-ray emission from this extragalactic object is not seen in the current *VERITAS* data (Aliu et al. 2014), thus making this association unlikely. Moreover, the unknown blazar is separated by 6.7 arcmin away from the centroid of VER J2016+371, which is much larger than $\sim$1.5 arcmin uncertainty of the *VERITAS* measurement (Aliu et al. 2014). In our present *Fermi-LAT* analysis, we have obtained best-fitting location of the source is about $0^{\circ}.04$ away from the 3FGL J2015.6+3709 and it is towards the location of the PWN supporting the association of the *Fermi-LAT* source with CTB 87 as well as with VER J2016+371.

5 CONCLUSION

We have seen that the observed spectrum from radio to TeV energies can be well explained by a leptonic scenario of a BPL and a Maxwellian distribution of electrons when the observed TeV fluxes from VER J2016+371 are associated with the positionally coincident counterparts at low energies. Specifically, the association of *Fermi-LAT* source with the TeV source indicates the presence of a Maxwellian distribution of electrons in the emission volume since the observed MeV–GeV fluxes are better explained by gamma rays from IC process for this electron distribution. In addition, a

hadronic scenario can also explain the observed GeV–TeV data for high density of the ambient medium. However, any strong observational evidences are not present to support this scenario as a significant scenario for this PWN. The dominant emission processes for VER J2016+371 are obtained considering its association with the sources at radio and X-ray energies. Angular accuracy for the measurements at radio and X-ray energies are far better than that of measurements at gamma-ray energies. Hence, future gamma-ray instruments with far better angular resolution (e.g. CTA) can provide significant information required to understand the spectral and spatial structure of the source and validity of these associations.

ACKNOWLEDGEMENTS

Data obtained from the High Energy Astrophysics Science Archive Research Center (HEASARC), provided by NASA's Goddard Space Flight Center is used in this work. LS acknowledges the use of Fermi-LAT data and analysis tool from Fermi Science Support Center. LS would like to thank the anonymous referee for his/her comments and suggestions, which improved the manuscript. This work was supported by the National Science Center (Poland), within the project DEC-2011/02/A/ST9/00256.

REFERENCES

Abdo A. A. et al., 2009, ApJS, 183, 46
Acero F. et al., 2015, ApJS, 218, 23
Ackermann M. et al., 2013, Science, 339, 807
Aharonian F., Atoyan A., 1995, Astropart. Phys., 3, 275
Aliu E., Aune T., Behera B., Beilicke M., Benbow W., Berger, 2014, ApJ, 788, 78
Amato E., Guetta D., Blasi P., 2003, A&A, 402, 827
Atoyan A. M., Aharonian F. A., 1996, MNRAS, 278, 525
Bednarek W., Bartosik M., 2003, A&A, 405, 689
Bednarek W., Protheroe R. J., 1997, Phys. Rev. Lett., 79, 2616
de Jager O. C., Harding A. K., 1992, ApJ, 396, 161
de Jager O. C. et al., 2009, preprint (arXiv:0906.2644)
Dickel J. R., Denoyer L. K., 1975, AJ, 80, 437
Duin R. M., Israel F. P., Dickel J. R., Seaquist E. R., 1975, A&A, 38, 461
Gaensler B. M., Slane P. O., 2006, ARA&A, 44, 17
Grondin M.-H., Romani R. W., Lemoine-Goumard M., Guillemot L., Harding A. K., Reposeur T., 2013, ApJ, 774, 110
Hester J. J., 2008, ARA&A, 46, 127
Hillas A. M. et al., 1998, ApJ, 503, 744
Kara E. et al., 2012, ApJ, 746, 159
Kargaltsev O., Rangelov B., Pavlov G. G., 2013, preprint (arXiv:1305.2552)
Kelner S. R., Aharonian F. A., Bugayov V. V., 2006, Phys. Rev. D, 74, 034018
Kothes R., Reich W., Foster T., Byun D.-Y., 2003, ApJ, 588, 852
Kothes R., Fedotov K., Foster T. J., Uyanıker B., 2006, A&A, 457, 1081
LaMassa S. M., Slane P. O., de Jager O. C., 2008, ApJ, 689, L121
Matheson H., Safi-Harb S., Kothes R., 2013, ApJ, 774, 33
Mathis J. S., Mezger P. G., Panagia N., 1983, A&A, 128, 212
Meyer M., Horns D., Zechlin H.-S., 2010, A&A, 523, A2
Pineault S., Chastenay P., 1990, MNRAS, 246, 169
Saha L., Bhattacharjee P., 2015, J. High Energy Astrophy., 5–6, 9
Sanchez D. A., Deil C., 2013, preprint (arXiv:1307.4534)
Slane P., Castro D., Funk S., Uchiyama Y., Lemiere A., Gelfand J. D., Lemoine-Goumard M., 2010, ApJ, 720, 266
Spitkovsky A., 2008, ApJ, 682, L5
Sun X. H., Reich P., Reich W., Xiao L., Gao X. Y., Han J. L., 2011, A&A, 536, A83
Wallace B. J., Landecker T. L., Taylor A. R., Pineault S., 1997, A&A, 317, 212
Wendker H. J., Higgs L. A., Landecker T. L., 1991, A&A, 241, 551
Zhang L., Chen S. B., Fang J., 2008, ApJ, 676, 1210

This paper has been typeset from a TEX/LATEX file prepared by the author.